

See discussions, stats, and author profiles for this publication at: <https://www.researchgate.net/publication/340150621>

Modeling and Experiment Verification of Transmissivity of Low-THz Radar Signal Through Vehicle Infrastructure

Article in IEEE Sensors Journal · March 2020

DOI: 10.1109/JSEN.2020.2982984

CITATIONS

26

6 authors, including:



Yang Xiao

University of Birmingham

5 PUBLICATIONS 54 CITATIONS

SEE PROFILE



Emidio Marchetti

University of Birmingham

29 PUBLICATIONS 359 CITATIONS

SEE PROFILE



Fatemeh Norouzian

University of Birmingham

40 PUBLICATIONS 448 CITATIONS

SEE PROFILE



Marina Gashinova

University of Birmingham

217 PUBLICATIONS 2,345 CITATIONS

SEE PROFILE

READS

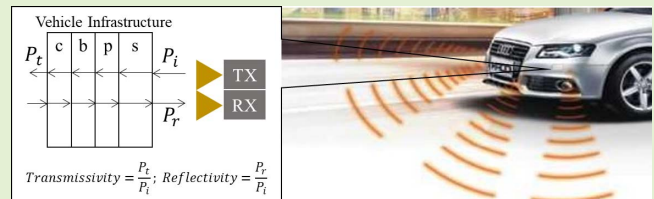
1,198

Modeling and Experiment Verification of Transmissivity of Low-THz Radar Signal Through Vehicle Infrastructure

Yang Xiao^{ID}, Fatemeh Norouzian^{ID}, Edward G. Hoare, *Senior Member, IEEE*, Emidio Marchetti, Marina Gashinova^{ID}, and Mikhail Cherniakov

Abstract—This paper is concerned with modelling of the transmissivity of Low-Terahertz waves through automotive bumper and headlight cover material. This work is part of wider comprehensive studies on the potential for the use higher frequency bands for future automotive sensors. Theoretical models for transmissivity prediction are described, the methodology of experimentation is discussed and experimental results are presented. The theoretical models of reflection and transmission of different base materials which are covered by different layers of paint are based on Fresnel theory, and the phenomena caused by the half wavelength thickness of the medium is analyzed mathematically. The experimental verification of the models in this paper have been undertaken at 300 GHz and 670 GHz, using 77 GHz as a reference frequency.

Index Terms—Sensor systems, automotive applications, submillimeter wave propagation, propagation losses, permittivity, automotive components, automotive materials.



I. INTRODUCTION

SINCE the first serious investigations into automotive radar were reported in the early 1970s, automotive sensors have become a key technology enabling intelligent and autonomous features in modern vehicles [1]. Over the last three decades, the development of automotive comfort and safety features has been a major objective for vehicle manufactures [2], [3] to solve the problems of human error and split-second decision making [4], [5]. Compared with other sensor technologies, such as light detection and ranging (LIDAR) and optical cameras [6], radar sensing has been identified as the most reliable all-weather technology for driver assistance applications, and has attracted considerable attention from researchers [7]. Radar can directly measure the range and velocity of objects with

reduced influence from environmental effects such as bad weather, lighting conditions, etc.

Generally, automotive radar sensors can be loosely classified as: long-range radar (LRR, 150 m), mid-range radar (MRR, 80 m) and short-range radar (SRR, 30 m) [8]. The three main frequency bands used in automotive radar applications are currently: 24 GHz, 76–77 GHz and recently introduced 77–81 GHz ultra-wide band (UWB) [9], [10]. Nevertheless, the increase of automotive radar frequency beyond the current bands can provide benefits [11]–[17] due to:

- Potential increase in the radar signal bandwidth leading to improvement in range resolution;
 - Reduction of antenna dimension when keeping the same angular resolution, alternatively increase in angular resolution having the same antenna dimension;
 - Increase in radar image quality due to higher sensitivity to target texture;
 - Increase in radar cross section (RCS) and less angular fluctuations of RCS [18];
 - Reduction of spectrum occupancy issues as traditional automotive bandwidths become more and more congested.
- Therefore, radars operating in the Low-THz frequency bands are being investigated as advanced sensing systems for future automotive sensor application [12], [19].

Manuscript received February 17, 2020; accepted March 8, 2020. Date of publication March 24, 2020; date of current version July 6, 2020. This work was supported by the Jaguar Land Rover and the U.K.-EPSRC as part of the jointly funded Towards Autonomy: Smart and Connected Control (TASCC) Programme under Grant EP/N012372/1. The associate editor coordinating the review of this article and approving it for publication was Prof. Piotr J. Samczynski. (Corresponding author: Yang Xiao.)

The authors are with the School of Electronic, Electrical and Systems Engineering, University of Birmingham, Birmingham B15 2TT, U.K. (e-mail: yxx752@student.bham.ac.uk).

Digital Object Identifier 10.1109/JSEN.2020.2982984

The THz frequency spectrum spans the frequency range between the infrared and microwave regions, and we will define Low-THz as the frequency band between 100 GHz and 1,000 GHz (1 THz). The generally believed disadvantage of automotive radars operating at these higher frequencies is increased atmospheric attenuation and attenuation through radome material, including additional contamination from water, leaves, ice etc. The attenuation due to sensor cover and contaminants is the subject of this investigation but the latest research shows that the band around 300 GHz is potentially applicable for LRR and definitely for MRR [18], [20]–[23]. However even higher frequencies could be effectively used as very high resolution automotive sensors for SSR.

Currently there is also significant interest in Low-THz operation in areas outside the automotive sensor application area [24], such as security [25] and medical imaging [26]. The feasibility of Low-THz radar for outdoor applications, such as automotive sensors, requires detailed investigation. Therefore, this paper discusses the practical aspects of Low-THz automotive sensors incorporated into the infrastructure of a vehicle.

Often automotive sensors are required to be invisibly installed behind different parts of the vehicle to fulfill design and styling requirements [27], [28]. For instance, sensors for autonomous cruise control (ACC), blind spot detection and rear collision warning are often installed behind the front and rear bumper material.

In this research, as shown in Fig. 1, we postulate that the radar sensors may be installed behind the bumper or headlight cover in the front of the vehicle. The sensor signal propagation loss in the path should be included into the radar equation as:

$$P_r = \frac{P_t G^2 \sigma \lambda^2 L_{co}}{(4\pi)^3 R^4}, \quad (1)$$

where L_{co} is the miscellaneous propagation losses which includes contributions from atmospheric propagation loss L_{ap} , the loss due to obscurants, L_w , attenuation in the sensor cover material, L_m , including the loss from contaminants on it, L_c , and any other factors in the path, L_{oth} . This total loss can be represented as:

$$L_{co} = L_{ap} L_w L_m L_c L_{oth} \quad (2)$$

The atmospheric propagation attenuation L_{ap} is influenced by humidity. According to the reported values in previous works, even in heavy rain, attenuation at 300 GHz does not typically exceed 10 dB/km, which will result in less than 4 dB two-way attenuation loss in the range of 200 m. The detail information of propagation loss in weather-related obscurants are given in works [29]–[31]. The parameter L_c relates to attenuation in various contaminants on the radome such as water, ice, sand, diesel, gasoline and fallen leaves. Attenuation due to such contaminants have been studied and can be found in [13], [20]–[22], [32].

In this paper, the attenuation caused by sensor covers L_m as one of the components of loss L_{co} is presented and described via the transmissivity of automotive bumpers and headlight covers. The investigation and optimization of the propagation performance of sensor covering material at 76–81 GHz has

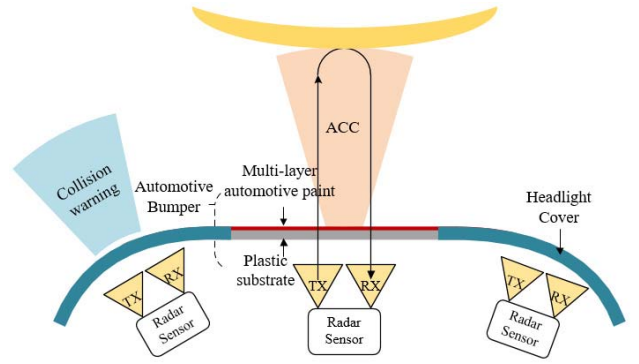


Fig. 1. Layout of potential automotive sensor installation. Radar sensors are placed behind the automotive bumper and the headlight cover.

been studied in several projects, such as the KOKON project [8] and the Radar-on-Chip for Cars (RoCC) project [33]–[36]. Therefore, conducting this new research at Low-THz frequencies is complimentary, and necessary, for considering Low-THz radar for automotive applications.

The theoretical part of this paper is based on Fresnel's equation and transmission line theory, which are commonly used in electromagnetic wave analysis [37]. However, utilizing this theory to estimate the performance of particular automotive component materials for Low-THz automotive sensor applications has not been reported before.

The main task of this paper is to establish an experimentally verified mathematical model of the transmission and reflection performance of potential automotive sensor covers at Low-THz. This will be valuable to predict performance degradation and assist the industrial design of sensor covers.

This paper is organized as follows. In section 2, the theoretical models of transmission of multi-layer structures are determined based on Fresnel's theory. The transmissivity simulations of headlight-cover (one-layer structure) and bumpers (four-layer structure) are based on this model. Also, the effect of the integer half wavelength electrical thickness of the medium on transmissivity and reflectivity is analyzed mathematically. The transmissivity is simulated through bumpers with different types of paint and the effect of various types of paint is analyzed. Section 3 introduces the measurement methodology, using a reference frequency of 77 GHz, and at the Low-THz 300 GHz and 670 GHz frequencies. All the experimental results are shown in Section 4. The effective permittivities of the vehicle component samples are estimated using the free space method. The measured and simulated transmissivities of automotive materials are compared and good agreement between them is obtained. The modelling in this paper is based on reflection and transmission coefficients for horizontal polarization, since the polarization of the antennas used in our experiments are horizontal.

II. ANALYTICAL MODELING

The general layout of infrastructure covering automotive sensors is shown in Fig. 1, and the modelling for multi-layer structure is introduced in this section as shown in Fig. 2. We assume that the cover is a stack of planar layers consisting of base material and different paints, each with its own physical

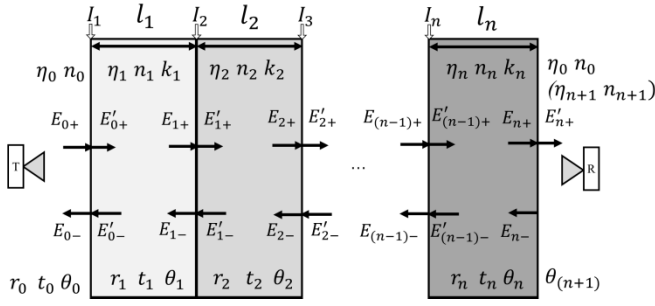


Fig. 2. The electric field in the propagation process through a multi-layer sample.

parameters and thickness. When radiation strikes a surface between air and the cover, part of the signal is absorbed, part of it is reflected, and the remaining part is transmitted through the cover material. The ratio of the reflected power to incident power is defined as “Reflectivity”, which indicates reflections from each interfaces inside the medium, and the fraction of the incident power that is transmitted through the medium is defined as “Transmissivity” which indicates the signal reduction as a result of absorption inside and reflections from each interface [13]. In part A, the transmissivity and reflectivity for the multi-layer medium and headlight cover are simulated at 77 GHz, 300 GHz and 670 GHz. The incident angle of the microwave signal and thickness of the medium at different frequency bands are considered as the variables of the transmissivity and reflectivity simulation. The phenomenon of periodic changes on simulated results, which will be shown in this section, is due to the interference between reflections from boundaries of the media. Transmissivity through automotive bumpers with different substrate material and various paints are investigated at 300 GHz and 670 GHz based on the complex permittivity of automotive paints measured by THz-time domain spectroscopy (TDS).

A. Theoretical Model of Transmission of Multi-Layer Structure Medium: “General Approach”

The theoretical model used to simulate transmissivity through multi-layer medium in this paper are based on Fresnel’s theory and calculation of propagation matrices in [38]. Similar standard method has been discussed in [13], [39], therefore for integrity and brevity of paper, we only outline this approach.

The propagation process through a multi-layer medium is shown in Fig. 2 where for simplicity only orthogonal incidence is shown. The notation of the parameters are as follow: η_i and k_i are the wave impedance and wave number in i th layer [13], r_i and t_i are reflection and transmission coefficient respectively at interface I_{i+1} , which can be determined using Fresnel equations as in [27]. E_{i+} , E_{i-} and E'_{i+} are the incident, reflected and transmitted electric fields. θ_i is the incident angle within each layer, defined by Snell’s law.

Based on the reflection and transmission coefficient and the electro-physical parameters of materials, the matrix of the electric field of the transmission process of multi-layer media is calculated by stacking the matching matrix M_{mi} of each

interface and the propagation matrix M_{pi} of each layer of media [40]:

$$\begin{aligned} \begin{bmatrix} E_{0+} \\ E_{0-} \end{bmatrix} &= M_{m0} \times M_{p1} \times M_{m1} \dots \times M_{pn} \times M_{mn} \begin{bmatrix} E'_{n+} \\ 0 \end{bmatrix} \\ &= \begin{bmatrix} A_{1,1} & A_{1,2} \\ A_{2,1} & A_{2,2} \end{bmatrix} \begin{bmatrix} E'_{n+} \\ 0 \end{bmatrix}. \end{aligned} \quad (3)$$

where $A_{i,j}$ represents the elements of the transmission matrix. The transmissivity and reflectivity are represented as:

$$T = \left| \frac{E'_{n+}}{E_{0+}} \right|^2 = \left| \frac{1}{A_{1,1}} \right|^2, \quad \Gamma = \left| \frac{E_{0-}}{E_{0+}} \right|^2 = \left| \frac{A_{2,1}}{A_{1,1}} \right|^2 \quad (4)$$

It is worth to stressing here that the transmissivity is only determined by parameter $A_{1,1}$ and an example of calculated $A_{1,1}$ and Eq. (3) for a three-layer structure is presented in Appendix A. The model for the transmissivity through the headlight-cover and the bumper is therefore based on general N-layer structure transmission matrix.

In a practical application, the radar signal propagates in a round trip and through the automotive components from both surfaces. For example, when a radar is installed behind the bumper, the signal will propagate from the plastic substrate to paint layer (forward path) for the first path and then from the paint layer to substrate (return path) when reflected back. Therefore, it is necessary to understand the relationship between the transmissivity of both cases theoretically.

The parameters without prime (θ_i, r_i, t_i) refers to “forward path” and parameters with prime (θ'_i, r'_i, t'_i) refers to “return path”. According to Snell’s law, ray angles of each interface are only determined by the refractive indices of two adjacent media. For non-magnetic materials, ray angles $\theta'_0, \dots, \theta'_{(n+1)}$ in the return path will be equal to the angles $\theta_{(n+1)}, \dots, \theta_0$ in the forward path. After representing the reflection and transmission coefficients of the return path, we can obtain the relationships between reflection and transmission coefficients for both cases to be $r'_i = -r_{n-i}$ and $\prod_{i=0}^n t_i = \prod_{i=0}^n t'_i$.

By calculating matrix Eq. (3) for both cases, we can obtain that the first element in the propagation matrix of both cases are equal: $A'_{1,1} = A_{1,1}$. The details are given in the Appendix B. Therefore, we can draw the conclusion that when a signal travels through the multi-layer sample in two opposite directions, the transmissivities are the same, the transmissivity value in a round trip can be obtained directly by just doubling transmissivity of one way through the medium. Hence all the results obtained in this study are directly applicable for radar scenario, i.e. two-way propagation.

B. Modeling Results of the Transmissivity Through Headlight-Cover. Single Layer Case

Headlight covers of vehicles are made of various materials of which polycarbonate (PC) is currently the most common. The simulated transmissivity through a headlight-cover based on the one-layer propagation matrices model is presented in this section. The values of complex permittivity of PC material at 77 GHz, 300 GHz and 670 GHz were obtained in [41]–[43] and are summarized in Table I. The imaginary part of refractive index k_e is calculated using the measured absorption coefficient α of PC material as described in [42], [43].

TABLE I
RANGES OF THE RELATIVE PERMITTIVITY OF PC AT 77 GHz,
300 GHz AND 670 GHz

| Frequency | 77 GHz | 300 GHz | 670 GHz |
|--------------|------------|-------------|-------------|
| ϵ' | 2.98—3.59 | 2.55—2.99 | 2.5—3.1 |
| ϵ'' | 0.02—0.053 | 0.039—0.052 | 0.058—0.066 |

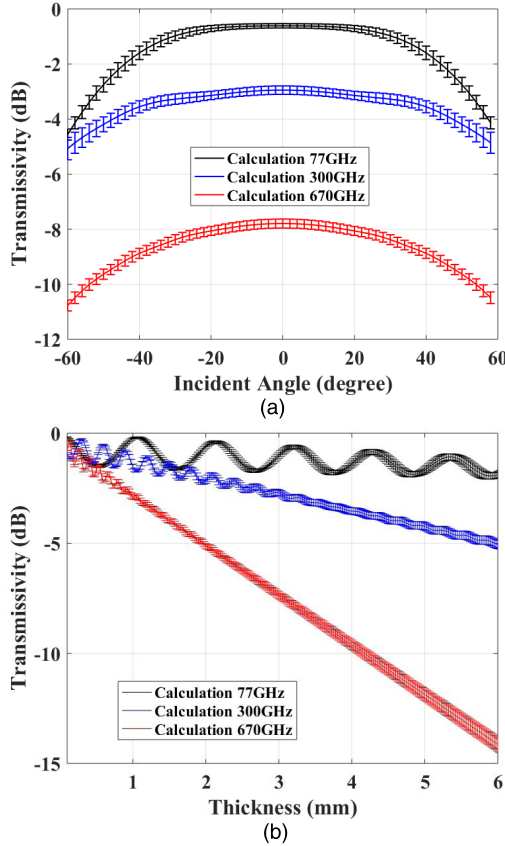


Fig. 3. Simulated transmissivity as a function of incident angle (a) and thickness (b) at 77 GHz, 300 GHz and 670 GHz.

The transmissivity (Fig. 3) and reflectivity (Fig. 4) of PC as a function of incident angle and the thickness of the medium are simulated for all the three frequencies. Error bars represent the uncertainty of transmissivity in the range of permittivity of PC as shown in Table I. The actual thickness of one used headlight-cover sample is 3.2 mm, which is used as the thickness parameter when simulating transmissivity and reflectivity as a function of incident angle. Transmissivity and reflectivity as function of thickness are simulated for 0° incidence.

Fig. 3 (a) illustrates that the simulated transmissivity through the headlight-cover at normal incidence is at approximately -0.6 dB, -3 dB and -8 dB at 77 GHz, 300 GHz and 670 GHz, respectively. At incident angles of $\pm 60^\circ$, the transmissivity is decreased by 4 dB, 2 dB and 3 dB at 77 GHz, 300 GHz and 670 GHz respectively. Fig. 3 (b) shows how transmissivity changes with thickness. For example, transmissivity decreases about -2 dB, -5 dB and -14 dB when the thickness increases from 0.1 mm to 6 mm at 77 GHz, 300 GHz and 670 GHz, respectively.

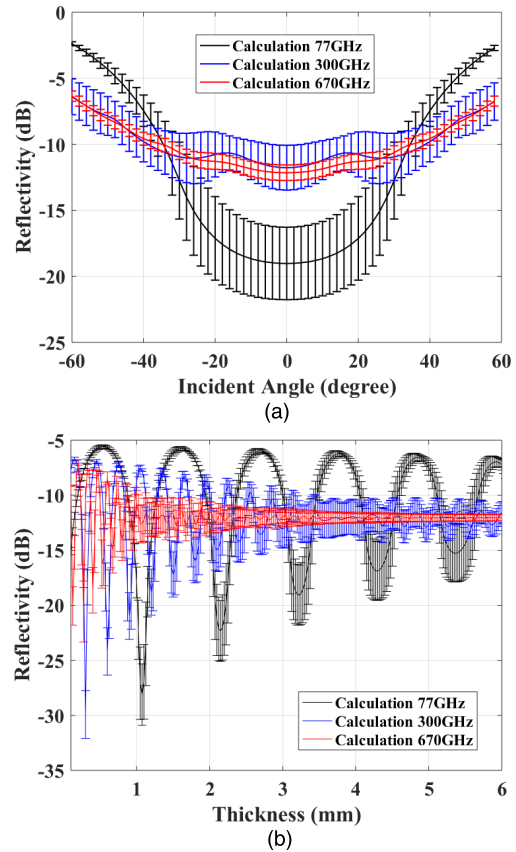


Fig. 4. Simulated reflectivity as a function of incident angle (a) and thickness (b) at 77 GHz, 300 GHz and 670 GHz.

Simulated values of transmissivity indicate periodic oscillations with amplitudes getting smaller with increase of frequency and/or thickness. Simulated reflectivity in Fig. 4 (b) shows similar trend where the depth of amplitude minima decreases with increased thickness.

Such oscillations relates to the changing ratios of half-wavelength and thickness of the propagation layer as explained below. Let us consider idealized and realistic scenarios of interference of two reflected waves from two interfaces of a single layer with the thickness equal to integer multiple of $\lambda_0/(2n)$ (n is the refractive index of the medium, λ_0 is the wavelength in vacuum) as shown in Fig. 5, where signal 1 (solid line) and signal 2 (dashed line) correspond to the reflected signals from the first and second interfaces. In the ideal case (no attenuation inside the layer), they entirely cancel each other. The power of the reflected signal is zero this case and transmissivity shows a maximum value. However, in the realistic case the reflected signal from the second boundary cannot totally cancel out the reflected signal from the first interface due to the attenuation inside the medium. Therefore, when the attenuation in the medium increases with increase of frequency, the amplitude of interference signal is bigger, indicating incomplete cancellation. Therefore, at the values of thickness corresponding to multiples of the half-wavelength the reflectivity will have reduced depth of the nulls with the increase of frequency.

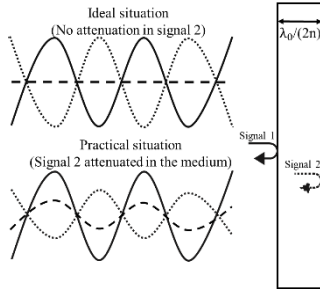


Fig. 5. Illustration of the interference between the signals reflected by both boundaries of the medium of thickness equal to integer multiple of the half-wavelength. Solid and dotted lines represent signal 1 and 2, respectively. Dashed line shows the result of interference of signals 1 and 2.

| |
|-------------------------------|
| Layer 4: Clear coat 25μm-40μm |
| Layer 3: Basecoat 15μm-50μm |
| Layer 2: Primer 4μm-25μm |
| Layer 1: Substrate 2mm-4mm |

Fig. 6. Sketch of four-layer bumper and the range of the thickness for each layer.

To prove this phenomenon mathematically, we can simplify the transmissivity equation for one-layer medium (4) as in (5):

$$T = \left| \frac{t_0 t_1 e^{-jk_1 l_1}}{1 + r_0 r_1 e^{-2jk_1 l_1}} \right|^2 = \left| \frac{2\eta_1 \eta_0}{(\eta_1^2 + \eta_0^2) j \sin(k_1 l_1) + 2\eta_1 \eta_0 \cos(k_1 l_1)} \right|^2, \quad (5)$$

where η_0 and η_1 are intrinsic impedances of wave in the medium and free space, respectively. They are defined as $\eta_i = \sqrt{\frac{j\omega\mu_i}{\delta_i + j\omega\epsilon_0\epsilon_i}}$, in which $\mu_0 = 4\pi \times 10^{-7}$, $\epsilon_0 = 8.854 \times 10^{-12}$ for free space and μ_1 and ϵ_1 are the permeability and relative permittivity of material, δ_i is the conductivity and ω is the frequency.

C. Modeling Results of the Transmissivity Through Bumper. Multi-Layer Case

Typically, modern bumpers are composed of three main elements: fascia, energy absorber and bumper beam [44], [45]. In this research, only the outside bumper fascia is considered as an obstacle for the radar signal propagation, which consists of the plastic substrate and paint layers. The layer structure of bumper and the thickness range for each layer are shown in Fig. 6. The materials of the substrate were reported to be Polypropylene (PP) and PC/Polyethylene terephthalate (PET) in [27] and [5], respectively. The plastic substrate is usually made of a combination of thermoplastic polymer, carbon black and talc. The complex permittivity of substrate layer depends on the composition of materials.

Three kinds of automotive paints commonly used in vehicles: solid paint, metallic paint and pearlescent paint. Generally, automotive paints include primer, basecoat and clear coat. The primer layer ensures better adhesion of paint, the

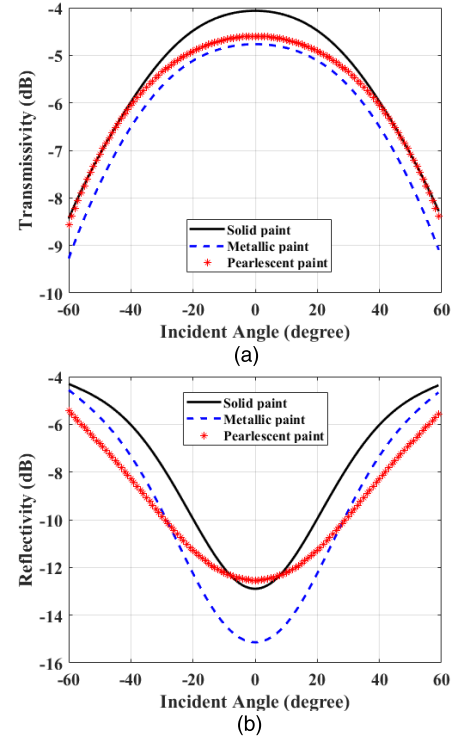


Fig. 7. The simulated transmissivity (a) and reflectivity (b) of four-layer bumper with solid, metallic and pearlescent paint at 77 GHz.

base coat layer is for color application and clear coat layer is used for protecting the paint from scratches and bad weather.

In this analytical section, we would like to understand the attenuation effects caused by various paint layers. To ensure that the only variable in this analysis is the paint layer, the substrate material is assumed to be PC, which is a commonly used vehicle plastic. The simulation structure consists of four layers: the substrate and the paint layers of primer, basecoat and clear coat. The permittivity parameters of PC are shown in Table I.

The permittivity values of primer, base coat and clear coat used in transmissivity and reflectivity simulation are presented in Table II. The 77 GHz values are obtained from previous work in [5], [46]. For Low-THz frequency range (300 GHz and 670 GHz), permittivity has been measured using the THz Time Domain Spectroscopy (TDS) setup at the University of Birmingham. TDS is a spectroscopic technique and utilize a short pulses of THz frequency radiation with a wideband spectrum, which is used widely to extract permittivity of large variety of materials [42], [47], [48]. For each simulation, the only variable of this simulation is the material of base coat paint layer that complex permittivity is extracted from solid, metallic and pearlescent paints respectively. Complex permittivity of plastic substrate, primer and clear coat are the same at each frequency. According to the measured permittivity values, as well as those reported in [5], metallic paint normally has a higher imaginary part of permittivity compared with solid and pearlescent paint because of the metal concentration. The simulated transmissivity and reflectivity of the bumper with three different kinds of base coat paint layer at 77 GHz, 300 GHz and 670 GHz are represented in Fig. 7, 8 and 9, respectively.

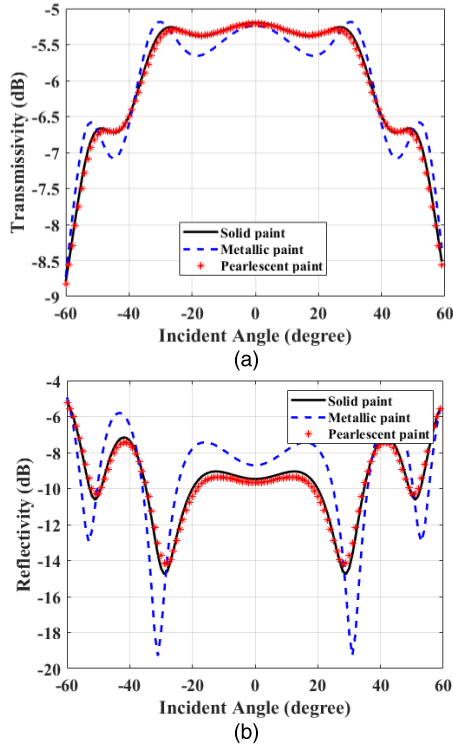


Fig. 8. The simulated transmissivity (a) and reflectivity (b) of four-layer bumper with solid, metallic and pearlescent paint at 300 GHz.

TABLE II

COMPLEX PERMITTIVITY OF MATERIALS USED IN SIMULATION

| Material | 77 GHz (ϵ_r/ϵ_i) | 300 GHz (ϵ_r/ϵ_i) | 670 GHz (ϵ_r/ϵ_i) | Thickness |
|-----------------------|---------------------------------------|--|--|------------|
| Plastic substrate | 2.98/0.1 | 2.75/0.045 | 2.8/0.062 | 4 mm |
| Primer | 9/0.06 | 5.29/0.08 | 5.15/0.12 | 25 μ m |
| Clear coat | 3.5/0.1 | 2/0.07 | 2.7/0.09 | 40 μ m |
| Solid base coat | 9.99/0.907 | 3.07/0.1 | 2.99/0.14 | 50 μ m |
| Metallic base coat | 5.99/1.609 | 4.94/0.2 | 5.14/0.6 | 50 μ m |
| Pearlescent base coat | 3.22/0.007 | 2.77/0.12 | 2.65/0.06 | 50 μ m |

According to Eq. (5), the amplitude of the minimum and maximum values of transmissivity and reflectivity are also influenced by the real part of permittivity, higher ϵ_{rel} values cause larger variations in the amplitude of transmissivity and reflectivity. This conclusion can be observed in the simulation result of metallic paint which has a higher real part of permittivity at 300 GHz. In addition, the metallic paint with higher dielectric loss factor also causes higher attenuation at both frequencies.

III. MEASUREMENT METHODOLOGY

The methodology to measure transmissivity through various samples at three frequencies is explained in this section. To obtain the transmissivity value, the transmitted signal strength through the automotive component samples is normalized by the transmissivity through free space in the below experiments. Fig. 10 (a) is a photo of the experimental setup for measuring transmissivity, Fig. 10 (b) is the measurement layout for the single path transmission measurement setup, which is commonly used for transmissivity measurement [28]. In the

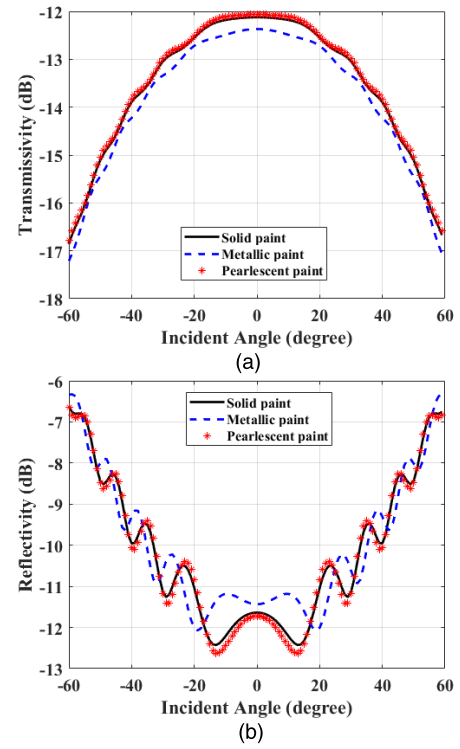


Fig. 9. The simulated transmissivity (a) and reflectivity (b) of four-layer bumper with different kinds of paint at 670 GHz.

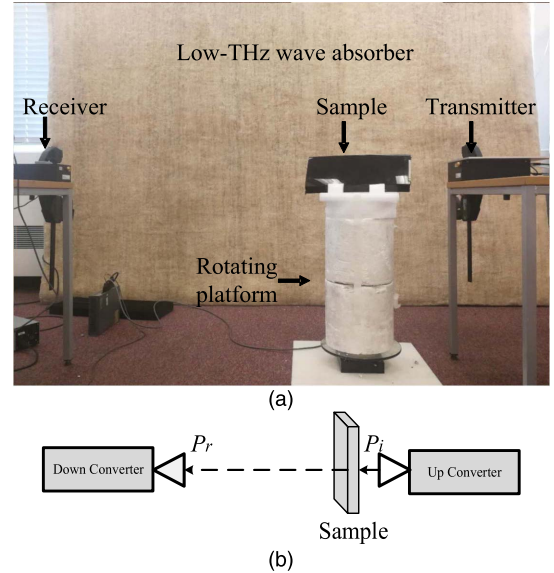


Fig. 10. (a): The experimental setup for measuring transmissivity. The radar system shown in the setup is 670 GHz SFR (stepped frequency radar). (b) Schematic diagram of the measurement setup.

main configuration the up and down-converters are positioned separately on two tables. The distance between receiver and transmitter is 1.4 m, and antennas of up and down converter are aligned vertically and horizontally. The antennas are placed 0.7 m above the floor level. The sample is fixed on a low reflectivity sample holder positioned on a rotating platform which can change the incident angle in 1° increments. The sample holder reflectivity has been measured as -33 dB and -21.2 dB at 300 GHz and 670 GHz, respectively. To ensure

TABLE III

PARAMETERS FOR 77 GHz, 300 GHz AND 670 GHz RADAR SYSTEMS

| Frequency | 77 GHz | 300 GHz | 670 GHz |
|---|----------------------|-------------|-------------|
| Radar classification | FMCW | SFR | SFR |
| Frequency Bandwidth | 76—81 GHz | 282—298 GHz | 656—672 GHz |
| PNA output power P_p | × | −15 dB | −15 dB |
| Transmitted power P_t | 15 dBm | 3 dBm | −10 dBm |
| Antenna Gain | 20 dB | 20 dB | 24 dB |
| Azimuth/Elevation Beam width (−3dB) | 10° | 10° | 10° |
| F_p (Frequency of signal from PNA) | CW experiment | × | 7 GHz |
| | Bandwidth Experiment | × | 2—18 GHz |
| F_t (Frequency of transmitted signal) | CW experiment | 77—77.1 GHz | 289 GHz |
| | Bandwidth experiment | 76—81 GHz | 282—298 GHz |
| | | | 656—665 GHz |

that most of the energy illuminates the material, the sample is positioned closer to transmitter to make sure that the sample is larger than the footprint of the illuminating beam. The beamwidth is defined by 3 dB main lobe of the radiation pattern. Extra attention has been paid to make sure the samples are orthogonal to the antennas horizontal baseline. The Low-THz wave absorber [49] is placed in front of the wall closest to the antennas to minimize reflections from the surrounding.

The distance between sample and transmitter is set to be 0.4 m at all frequencies to guarantee that the experiment is conducted in far-field region. In real applications, the sensor covers will be closer to the antennas, so that the near-field effects may be expected. However, in this paper far field set-up is considered to provide a reference for validation of the modelling results. The near field effects and corresponding corrections to the modelling are subject of further research.

All measurements are made at three frequencies: two stepped frequency radars (SFRs) with the sweep frequency of 282 GHz—298 GHz and 656 GHz—672 GHz, and one FMCW radar system with the frequency coverage of 76 GHz—81 GHz using standard gain horn antennas.

The SFR systems are based on the KEYSIGHT programmable network analyzers (PNA) and the up and down converters designed by VivaTech in collaboration with University of Birmingham [50]. The signal from the PNA is up-converted into frequency of F_t and transmitted through the bumper sample under measurement. S_{21} parameter of the down converted signal is measured to obtain the transmissivity value. A 10 MHz reference signal is provided from a Rubidium oscillator to phase lock the converters and PNA.

The 77 GHz FMCW radar system is designed by ELVA-1 in collaboration with University of Birmingham [51]. All the frequency, power and antenna parameters are shown in Table III for all the radar systems.

Three variable parameters are considered in this paper to evaluate transmissivity: incident angle of signal, frequency and thickness of medium. The influence of the initial two variables are explored by measuring the transmissivity of bumpers and headlight-cover as a function of incident angle and frequency as the thickness remains constant. However,

to investigate the third variable, PC sheets with thicknesses ranging from 2 mm to 6 mm are measured. A CW signal is used to measure transmissivity versus incident angle and thickness, and bandwidth signal is used to understand the frequency dependence. As shown in Table III, F_t for the CW experiment at 77 GHz the bandwidth is 100 MHz since this is the minimum operational bandwidth of the FMCW radar.

IV. EXPERIMENTAL RESULTS

In this section, the measured and simulated transmissivity of car bumper and headlight cover material, as well as PC sheets of different thicknesses, are shown as a function of incident angle and frequency. Bumper samples with three kinds of paints and one piece of headlight-cover are measured to determine the transmissivities of these vehicle components. The effective permittivity is obtained using the free space method [52] based on the measured transmissivity as function of incident angle. The effective permittivity is used for modelling the transmissivity versus frequency bands. Various thicknesses of PC sheets are used to replicate common plastic material used as headlight covers.

A. Measured Transmissivity Through Automotive Bumpers and Headlight-Covers

Ten bumper samples and one headlight-cover have been used in experimentation. The material information is presented in Table IV, Appendix C, samples A to K.

The multi-layer transmissivity model requires the exact knowledge of permittivity of materials and the thickness of each layer. The exact refractive index of each layer of paint on the samples, at Low-THz frequencies, are unknown and in addition the thicknesses of the paint layers are difficult to measure without knowing the exact refractive indexes of the materials [53]. Consequently, a model of the transmissivity through a four-layer bumper cannot be directly established at this stage. Therefore, a one-layer structure, with the effective permittivity of the whole sample, is used to model transmissivity through the bumper material. The effective permittivities of the bumper samples are calculated using the measured transmissivity and used for further modelling.

There are two common methods to characterize the permittivity of the samples: (i) TDS is used for THz frequency (usually more than 300 GHz), and (ii) the free-space method [52] which uses a Vector Network Analyzer (VNA) is used for lower frequencies [54]. In this paper, the effective relative permittivity is determined using the method described in [13], by minimization of the deviation between the measured and simulated transmissivity results. The deviation, Dev , between the simulated transmissivity T_c and the measured transmissivity T_m , is obtained as:

$$Dev(\epsilon'_r, \epsilon''_r) = \sum_{i=1}^{120} |T_m(\theta_i) - T_c(\theta_i, \epsilon'_r, \epsilon''_r)|, \quad (6)$$

in which, θ_i is the incident angle of the microwave signal which is in range of -60° to 60° , ϵ'_r and ϵ''_r are the real and imaginary parts of the complex effective permittivity. Therefore, the effective permittivity is obtained by searching the minimum value of Dev integrated over the whole range

TABLE IV

CHARACTERISTICS OF AUTOMOTIVE SAMPLES, AND THE EFFECTIVE PERMITTIVITY ($\epsilon_r - j\epsilon_i$) AND TRANSMISSIVITY AT 0° (REPRESENTED AS T (0°)) OBTAINED FROM EXPERIMENTS. PP: Polypropylene; E/P: Ethylene / Propylene; PUR: polyurethane; PC: polycarbonate

PP: Polypropylene; E/P: Ethylene / Propylene; PUR: polyurethane; PC: polycarbonate

| Sample | Paint Classification | Size (m ²) | D (mm) | Plastic | 77 GHz | | | 300 GHz | | | 670 GHz | | |
|--------|----------------------|------------------------|--------|---------|---------------|----------------|---------|---------------|----------------|---------|---------------|----------------|---------|
| | | | | | ϵ'_r | ϵ''_r | T(0°) | ϵ'_r | ϵ''_r | T(0°) | ϵ'_r | ϵ''_r | T(0°) |
| A | Solid Black | 0.057 | 2.87 | PP,E/P | 4.02 | 0.035 | −0.5 dB | 2.48 | 0.025 | −1.9 dB | 3.36 | 0.020 | −2.8 dB |
| B | Solid White | 0.076 | 3.72 | PP,E/P | 4.34 | 0.030 | −0.7 dB | 3.00 | 0.021 | −2.1 dB | 4.26 | 0.022 | −3.0 dB |
| C | Solid White | 0.045 | 3.33 | PP,E/P | 5.38 | 0.042 | −1.5 dB | 2.78 | 0.036 | −2.4 dB | 3.37 | 0.038 | −4.1 dB |
| D | Solid White | 0.095 | 3.02 | PP,E/P | 4.29 | 0.022 | −2.0 dB | 3.76 | 0.033 | −2.7 dB | 3.24 | 0.019 | −2.0 dB |
| E | Metallic Gold | 0.078 | 3.15 | PP,E/P | 5.65 | 0.025 | −1.0 dB | 3.68 | 0.043 | −3.1 dB | 2.30 | 0.043 | −5.8 dB |
| F | Metallic Grey | 0.090 | 3.26 | PP,E/P | 4.58 | 0.003 | −2.0 dB | 4.80 | 0.051 | −2.7 dB | 5.00 | 0.042 | −6.0 dB |
| G | Pearlescent Red | 0.040 | 3.25 | PP,E/P | 3.50 | 0.026 | −1.0 dB | 2.91 | 0.039 | −2.5 dB | 3.00 | 0.040 | −5.0 dB |
| H | Pearlescent Red | 0.038 | 3.33 | PP,E/P | 5.73 | 0.023 | −0.2 dB | 3.50 | 0.024 | −1.3 dB | 3.60 | 0.036 | −4.6 dB |
| I | Pearlescent Green | 0.065 | 3.27 | PP,E/P | 3.49 | 0.029 | −0.6 dB | 2.54 | 0.024 | −1.3 dB | 2.65 | 0.014 | −3.0 dB |
| J | Pearlescent White | 0.074 | 3.34 | PUR | 6.95 | 0.040 | −5.8 dB | 2.63 | 0.120 | −7.4 dB | 3.74 | 0.186 | −20 dB |
| K | Headlight-cover | 0.057 | 3.20 | PC | 3.55 | 0.019 | −0.4 dB | 2.60 | 0.043 | −2.4 dB | 2.52 | 0.058 | −7.9 dB |

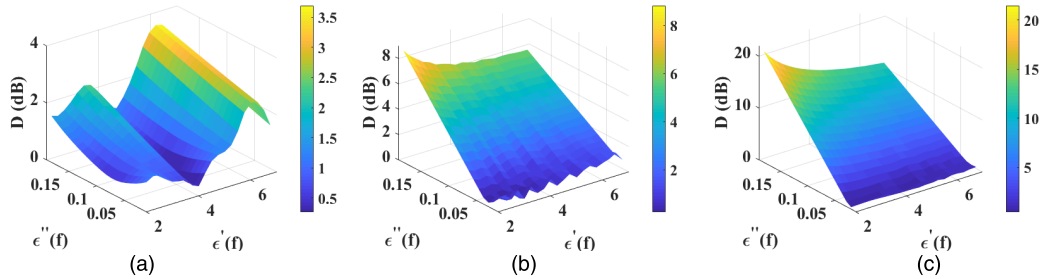


Fig. 11. The deviations between the simulated and measured transmissivities of sample “A” versus the possible range of real and imaginary part of permittivity at (a) 77 GHz, (b) 300 GHz and (c) 670 GHz.

of the incident angles in the defined possible range of effective permittivity values. The calculated Dev of sample A is shown in Fig. 11 as an example. The detail of the calculation process is represented in work [13]. The calculated effective permittivity of sample A which correspond to the minimum deviations are $4.02 - 0.035i$, $2.48 - 0.025i$ and $3.36 - 0.019i$ at 77 GHz, 300 GHz and 670 GHz, respectively. All the effective permittivities of the samples fall into the range of ϵ'_r : 2 – 7, ϵ''_r : 0.01 – 0.19 at three frequency bands of 77 GHz, 300 GHz and 670 GHz.

The effective permittivity for all samples is calculated using the technique described above. The experimental and simulated results as a function of incident angle at 77 GHz, 300 GHz and 670 GHz are illustrated in Fig. 12. The cases ((a)–(k)) correspond to different samples explained in Table IV, Appendix C. The property information of all the samples, measured effective permittivity and measured transmissivity at normal incidence at the three frequencies under study is summarized in Table IV, Appendix C.

In Fig. 13, the measured and simulated transmissivities of all samples as a function of frequency within a specific

operational bandwidth are shown. Due to similar observed trends for all samples, only results for two extreme samples D (metallic paint) and E (solid paint) are presented here. The effective permittivity used in this simulation is obtained from the measured transmissivity versus incident angle. Good agreement between the simulated and measured results as a function of frequency is achieved.

In Fig. 12 and Fig. 13, solid lines with error bars represent the measured results and the dashed lines correspond to the simulated results. Error bars represent the standard deviations for three individual measurements.

The overall trend of the measured transmissivity results versus incident angle shows that typically the transmissivity decreases as the frequency increases. However, for sample D, higher transmissivity is measured at 670 GHz compared to the result at 300 GHz in the angle range of $\pm 20^\circ$. The increase of transmissivity at this angle is observed because the electrical thickness of sample D at 670 GHz is close to integer values of half-wavelength at 0° incident angle. Electrical thickness of the layer is defined as $t_e = nd/\sin(\alpha)$, where n and d are the refractive index and the thickness of material, respectively,

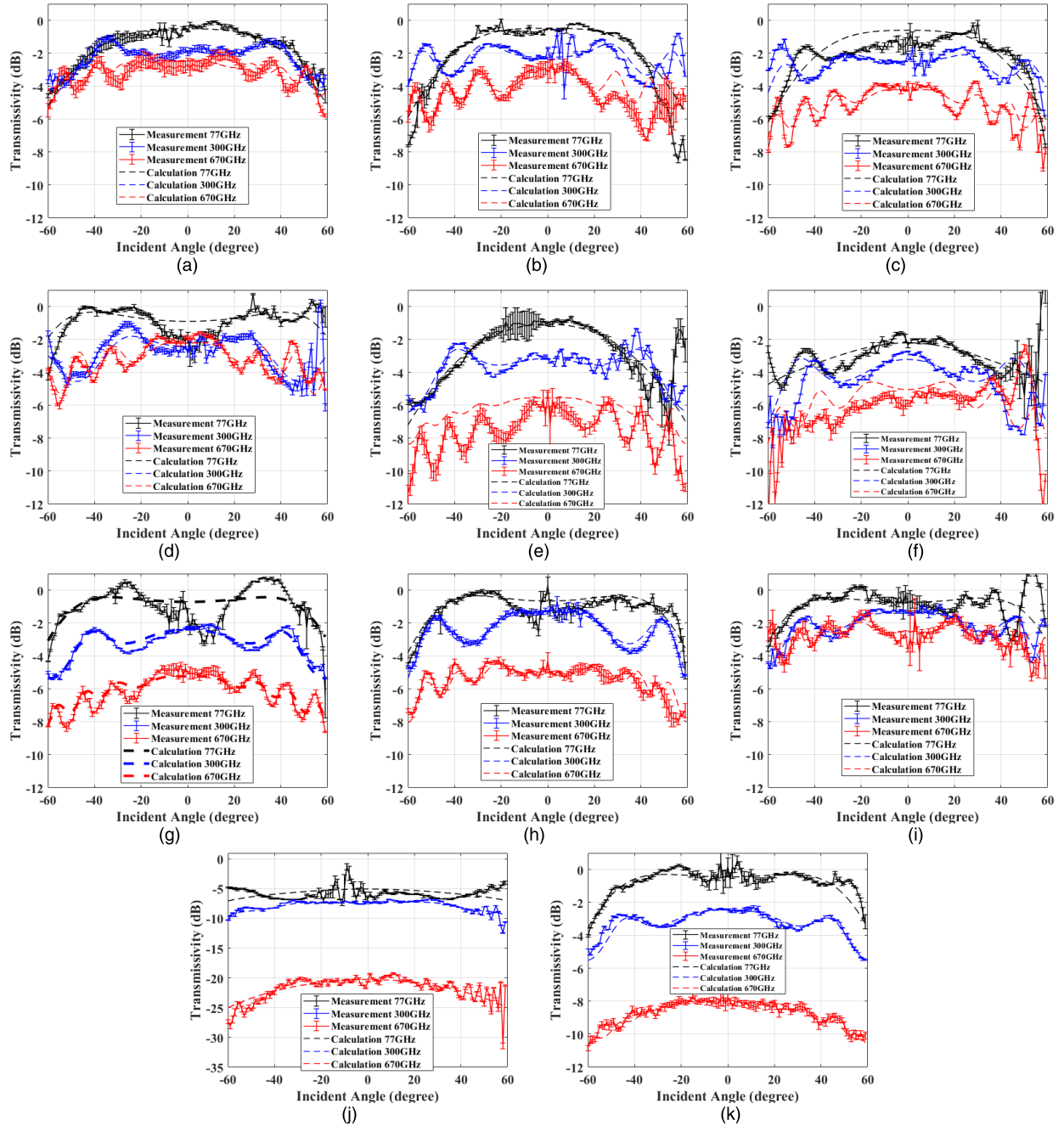


Fig. 12. Simulated and measured transmissivities of the automotive components as a function of incident angle using CW signal. Results in the frequency ranges of 77 GHz, 300 GHz and 670 GHz are represented in black, blue and red lines, respectively. (a)–(d) are results for bumper samples with solid paint, (e)–(f) are results for bumpers with metallic paint, (g)–(j) are results for bumpers with pearlescent paint and (k) is the result for headlight-cover.

α is the angle between beam propagation direction and the medium boundary. A series of calculation were conducted to analyze this phenomenon in section II (A). The extremes of the measured transmissivity as a function of incident angle are observed as expected. The electrical thickness of the sample changes with the incident angle due to different propagation path length. The constructive interference case is observed when $\frac{N\lambda}{2} = \frac{nd}{\sin(\alpha)}$, and N is integer factor. Shorter wavelength means shorter period of oscillations as the incident angle changes the length of propagation path inside the medium.

This observation illustrates the requirement for precision in the placement of the radar behind the covers at higher frequencies and consideration of the profile.

The measured transmissivity values at 0° incident angle for the three frequencies are shown in Fig. 14. The measured transmissivity through bumper samples with solid paint (A–D) shows a difference of approximately 1 dB between the three frequencies, this is well inside the measurement accuracy. However, for the bumpers with metallic paint (E–F) and pearlescent paint (G–J), the difference between the

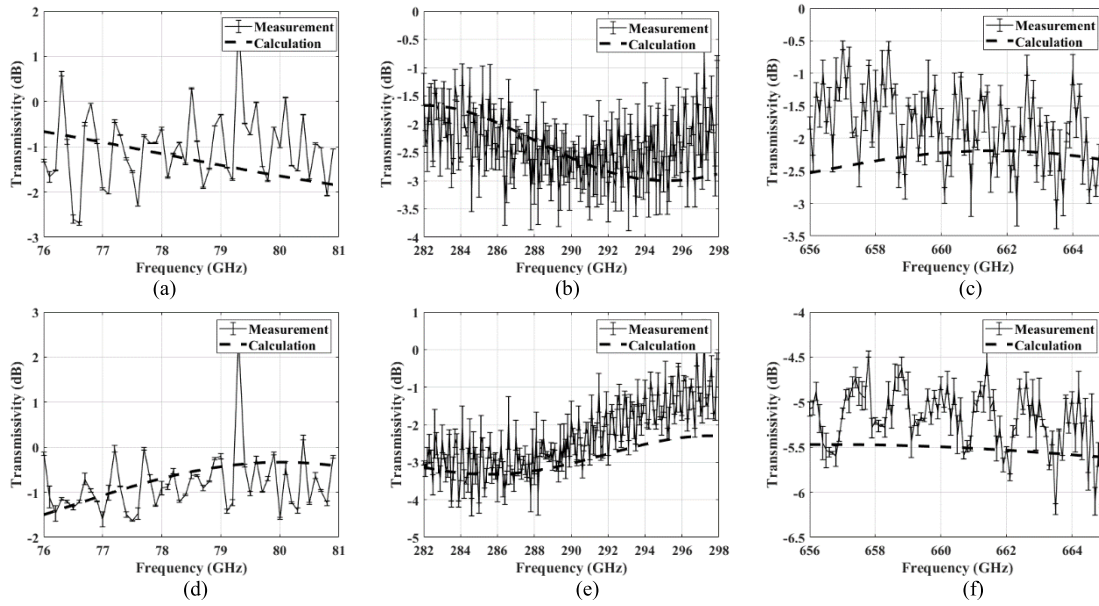


Fig. 13. Simulated and measured transmissivity of sample D and E vs frequency over a specific operational bandwidth: (a) (b) (c) are results for sample D at 77 GHz, 300 GHz and 670 GHz, respectively; (d) (e) and (f) are results for sample E.

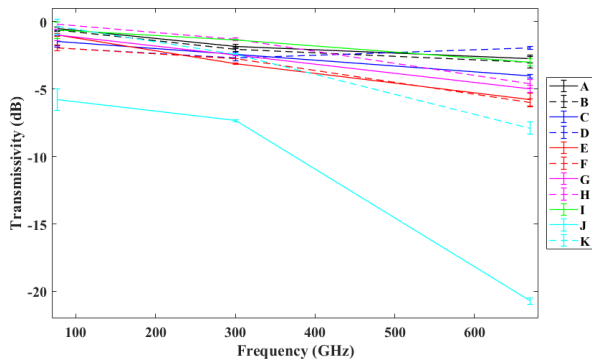


Fig. 14. Summary of the transmissivity at 0° incidence of the vehicle samples at 77 GHz, 300 GHz and 670 GHz.

transmissivity at 77 GHz and 300 GHz is higher than the difference between 300 GHz and 670 GHz, although the wavelength at 300 GHz is four times shorter than 77 GHz and wavelength at 670 GHz is only around two times shorter than 300 GHz. Considering sample G as an example, the transmissivity difference between 77 GHz and 300 GHz is around 1 dB which is smaller than the 3 dB difference between 300 GHz and 670 GHz.

The results of most bumper samples (except sample J) show that the transmissivity through metallic paint samples (E and F) are lower than that of solid and pearlescent paints in all the three frequency bands, even though the thickness of sample E and F are smaller than most of the other bumpers samples (except A and D). Results of sample J are observed to have more attenuation than the other samples as the substrate material of this sample is made of polyurethane (PUR) plastic, which is different to the others. Sample K is an optically transparent headlight-cover. The attenuation property of the headlight cover is at a similar level to the other samples at 77 GHz and 300 GHz, but decreases to -7.9 dB at 670 GHz, which is worse than the bumper samples with substrate material of PP.

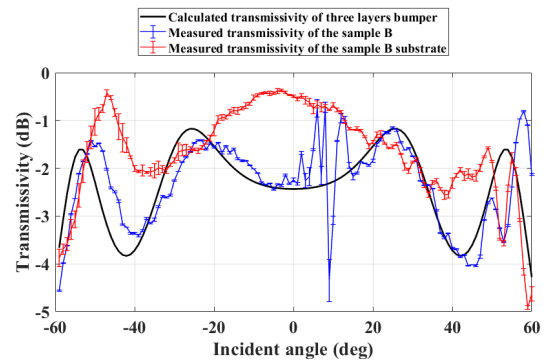


Fig. 15. Comparison of the simulated transmissivity of three-layer bumper and the measured transmissivity of sample B and the substrate of sample B.

Although precise multi-layer model of bumpers was difficult to establish because of the lack of information on the thickness of each paint layer, we still made some effort to compare the measurement results with the simulated transmissivity of multi-layer structures. To understand the transmissivity corresponding to the substrate plastic and the paint layers separately, the paint layer of sample B was removed and the transmissivity through sample B with no paint was measured.

Fig. 15 shows the measured transmissivity through sample B with paint (blue line) and without paint (red line) at 300 GHz, as well as the simulated transmissivity of three-layer bumper at this frequency (black line). The permittivity of substrate plastic layer is obtained from the measured result of bumper without paint based on the root searching method in section IV (A) [13], which is calculated to be $2.8-0.011i$ at 300 GHz. The permittivity of the primer and the white base coat paint are measured using TDS. The thickness of the substrate of sample B was measured at 3.62 mm. The thicknesses of primer and base coat layer are assumed to be $25 \mu\text{m}$ and $50 \mu\text{m}$ in this simulation, which is the maximum

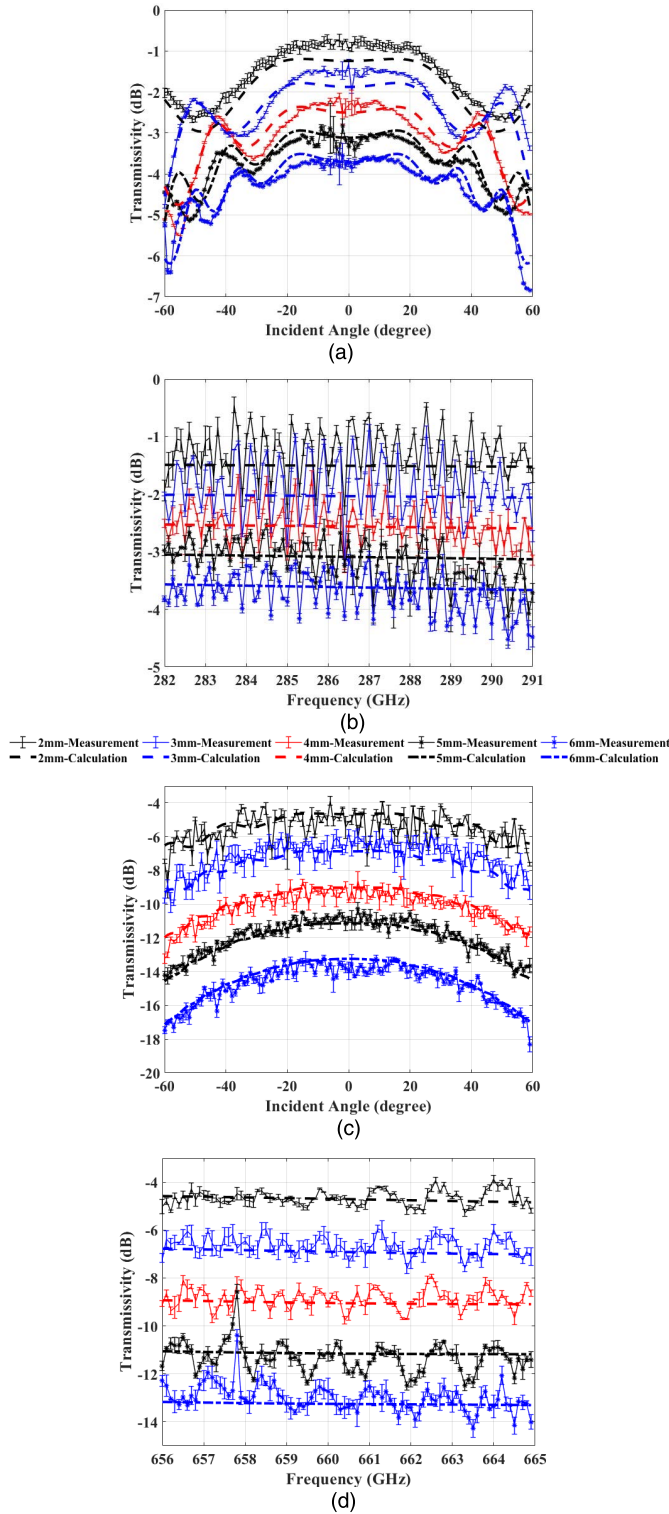


Fig. 16. Measured and simulated transmissivities through PC sheets with different thicknesses. (a) (b) are results at 300 GHz, and (c) (d) are results at 670 GHz. The inscriptions for these four results are the same as shown in the middle.

value in the thickness ranges shown in Fig. 6. Based on this permittivity and thickness information, the model of a three-layer structure bumper is established according to the theory in the theoretical section. The simulated transmissivity of the three-layer bumper of sample B is shown as a black line in Fig. 15, which agrees well with the measured results.

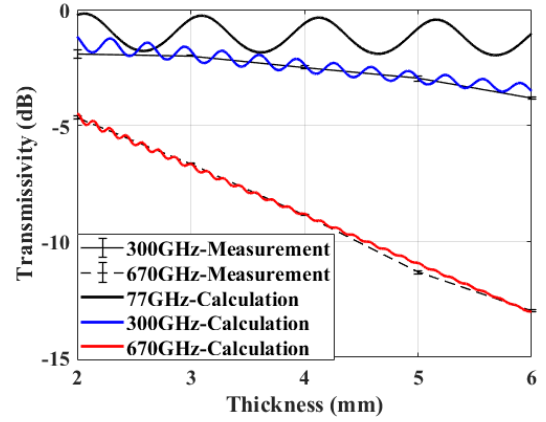


Fig. 17. The comparison of simulated and measured results as a function of medium thickness.

B. Transmissivity of PC Sheets With Different Thicknesses

The theoretical model of transmissivity and thickness is explored here using PC material which could be custom designed in different thicknesses. In this section, we will present experimental results on transmissivity depending on thickness, angle of incident and frequency and compare with results of simulation shown in section II before. The analysis in this section is concentrated on 300 GHz and 670 GHz only and this is for two reasons: (i) the main purpose of this research is to investigate the feasibility of automotive radar in the Low-THz frequency range and (ii) the theoretical simulation agrees well with the measurement results at 77 GHz in the previous sections and this gives confidence to rely on the theoretical simulation for comparison purposes.

The transmissivity of PC sheets with different thicknesses are measured and compared with theoretical simulations. PC sheets used are 2 mm, 3 mm, 4 mm, 5 mm and 6 mm in thicknesses and with the sheet dimension of 600 mm × 500 mm which guarantees that the sample covers the 3 dB beamwidth of the signal in both paths. Fig. 16 shows the measured and simulated transmissivity results through PC sheets as a function of incident angle and frequency.

The effective permittivity of PC sheets obtained by the root searching process are 2.5–0.032j and 2.6–0.057j at 300 GHz and 670 GHz, respectively. The measured and simulated transmissivity as a function of thickness at 300 GHz and 670 GHz are illustrated in Fig. 17. The simulated transmissivity through PC sheet with various thicknesses at 77 GHz are also presented for comparison. The simulated and measured results agree well in all the three plots at both frequencies. As the thickness increases from 2 mm to 6 mm, the transmissivity through PC sheets decreases from –1.5 dB to –3.5 dB at 300 GHz. However, at 670 GHz, the transmissivity decreases from –5 dB to –13 dB. As discussed in section II (B), smaller variation between local minima and maxima are observed when increasing thickness and frequency.

V. CONCLUSION

To estimate the propagation loss of potential automotive radar sensor covers, the measured and simulated transmissivity of automotive bumper material, headlight-cover material and

also PC sheets with different thicknesses are presented at Low-THz frequencies as a function of incident angle and frequency in this paper. Measured results at 77 GHz are also shown for comparison. Good agreement is found between the measured results and the theoretical modelling results which are based on Fresnel theory and propagation matrices. The effective permittivity of multi-layer bumpers and one-layer headlight cover are determined using the free space method. The measured results show bumpers with metallic paints have higher loss compared with solid paint and pearlescent paint bumpers and this is due to the metal composition. The losses through the bumper with a substrate composed of PUR plastic are measured, which are around 3 dB, 4 dB and 15 dB higher than the PP plastic substrate at 77 GHz, 300 GHz and 670 GHz, respectively. When radar sensor signals pass through the bumpers at 0° incident angle, the transmissivity is in the range of $-0.2 \text{ dB} \sim -5.8 \text{ dB}$, $-1.3 \text{ dB} \sim -7.4 \text{ dB}$ and $-2 \text{ dB} \sim -20 \text{ dB}$ at 77 GHz, 300 GHz and 670 GHz, respectively. The transmissivity through various thicknesses of PC sheets are measured and analysed as it is the main material of headlight covers and also some other parts of the vehicle components. The results show higher losses with increasing thickness at 670 GHz compared to 300 GHz, and a decrease with a step of 0.5 dB and 2 dB is measured at 300 GHz and 670 GHz, respectively, when the thickness increases in 1 mm increments. The results are directly applicable to automotive radar and also to wider applications in communication and other systems operating at Low-THz frequencies.

Two main conclusions can be drawn to aid the industrial design of sensor cover infrastructure: Firstly, the model correctly describes the transmissivity and reflectivity fluctuations as function of signal frequency, thickness of medium and the real part dielectric permittivity of constituent materials. Second (and obvious) conclusion is that the larger loss tangent of cover material, defined by the imaginary part of the dielectric permittivity, leads to higher absorption inside the medium and therefore high attenuation in the sensor cover.

When conducting industrial design of sensor covers, the permittivity, thickness, operating frequency and placement need to be properly matched to obtain low reflectivity and high transmissivity based on the developed theoretical model.

Further study will be taken to understand the impact of presence of bumper within the propagation path on phase noise of the transceiver [55].

APPENDICES

In the appendices section, we consider a three-layer medium as the example for calculation. The equations in this part have the substitution relationship of $\varphi_i = k_i l_i \cos \theta_i$.

A. Details of the Transmission Matrix Calculation

The detail of matrix calculation of transmission process (Eq. (3)) for three-layer medium are represented below as an

example:

$$\begin{aligned} \begin{bmatrix} E_{0+} \\ E_{0-} \end{bmatrix} &= \frac{1}{t_0} \begin{bmatrix} 1 & r_0 \\ r_0 & 1 \end{bmatrix} \times \begin{bmatrix} e^{j\varphi_1} & 0 \\ 0 & e^{-j\varphi_1} \end{bmatrix} \times \frac{1}{t_1} \begin{bmatrix} 1 & r_1 \\ r_1 & 1 \end{bmatrix} \cdots \\ &\times \begin{bmatrix} e^{j\varphi_3} & 0 \\ 0 & e^{-j\varphi_3} \end{bmatrix} \times \frac{1}{t_3} \begin{bmatrix} 1 & r_3 \\ r_3 & 1 \end{bmatrix} \begin{bmatrix} E'_{3+} \\ 0 \end{bmatrix} \\ &= \begin{bmatrix} A_{1,1} & A_{1,2} \\ A_{2,1} & A_{2,2} \end{bmatrix} \begin{bmatrix} E'_{3+} \\ 0 \end{bmatrix}, \end{aligned} \quad (7)$$

where $A_{1,1}$ is represented as:

$$\begin{aligned} A_{1,1} &= \frac{1}{t_0 t_1 t_2 t_3} (e^{j\varphi_1} e^{j\varphi_2} e^{j\varphi_3} + r_0 r_1 e^{-j\varphi_1} e^{j\varphi_2} e^{j\varphi_3} \\ &+ r_1 r_2 e^{j\varphi_1} e^{-j\varphi_2} e^{j\varphi_3} + r_0 r_2 e^{-j\varphi_1} e^{-j\varphi_2} e^{j\varphi_3} \\ &+ r_2 r_3 e^{j\varphi_1} e^{j\varphi_2} e^{-j\varphi_3} + r_0 r_1 r_2 r_3 e^{-j\varphi_1} e^{j\varphi_2} e^{-j\varphi_3} \\ &+ r_1 r_3 e^{j\varphi_1} e^{-j\varphi_2} e^{-j\varphi_3} + r_0 r_3 e^{-j\varphi_1} e^{-j\varphi_2} e^{-j\varphi_3}) \end{aligned} \quad (8)$$

B. Comparison of Propagation Matrix When Signal Incident From Two Opposite Directions of Medium

As mentioned in section II (A), the parameters without prime (θ_i, r_i, t_i) refer to “forward path” and parameters with prime (θ'_i, r'_i, t'_i) refer to “return path”. The characteristic parameters of materials for different layers for forward path are the same with return path. The reflection and transmission coefficients of return path are denoted as:

$$r'_i = \frac{\eta_{n-i} \cos \theta_{n+1-i} - \eta_{n+1-i} \cos \theta_{n-i}}{\eta_{n-i} \cos \theta_{n+1-i} + \eta_{n+1-i} \cos \theta_{n-i}} \quad (9)$$

$$t'_i = \frac{2\eta_{n-i} \cos \theta_{n+1-i}}{\eta_{n-i} \cos \theta_{n+1-i} + \eta_{n+1-i} \cos \theta_{n-i}} \quad (10)$$

Therefore, comparing with reflection and transmission coefficient for forward path, we can obtain the equal relationships: $r'_i = -r_{n-i}$ and $\prod_{i=0}^n t_i = \prod_{i=0}^n t'_i$. The propagation matrix of return path for three-layer structure can be represented as:

$$\begin{aligned} \begin{bmatrix} E_{0+} \\ E_{0-} \end{bmatrix} &= \frac{1}{t_0 t_1 t_2 t_3} \begin{bmatrix} 1 & -r_3 \\ -r_3 & 1 \end{bmatrix} \times \begin{bmatrix} e^{j\varphi_3} & 0 \\ 0 & e^{-j\varphi_3} \end{bmatrix} \\ &\times \begin{bmatrix} 1 & -r_2 \\ -r_2 & 1 \end{bmatrix} \cdots \times \begin{bmatrix} e^{j\varphi_1} & 0 \\ 0 & e^{-j\varphi_1} \end{bmatrix} \\ &\times \begin{bmatrix} 1 & -r_0 \\ -r_0 & 1 \end{bmatrix} \begin{bmatrix} E'_{3+} \\ 0 \end{bmatrix} = \begin{bmatrix} A'_{1,1} & A'_{1,2} \\ A'_{2,1} & A'_{2,2} \end{bmatrix} \begin{bmatrix} E'_{3+} \\ 0 \end{bmatrix} \end{aligned} \quad (11)$$

After extending the propagation matrix (Eq. (3) and (12)), the transmissivity equation for both two cases (T and T' are the transmissivity for forward and return path respectively) are the same as shown in Eq. (12), shown at the bottom of this page.

C. Bumper Material Information and Measured Effective Permittivities

See Table IV

$$\begin{aligned} T &= T' \\ &= \left| \frac{t_0 t_1 t_2 t_3 e^{-j\varphi_1} e^{-j\varphi_2} e^{-j\varphi_3}}{1 + r_0 r_1 e^{-j2\varphi_1} + r_1 r_2 e^{-j2\varphi_2} + r_0 r_2 e^{-j2\varphi_1} e^{-j2\varphi_2} + r_2 r_3 e^{-j2\varphi_3} + r_0 r_1 r_2 r_3 e^{-j2\varphi_1} e^{-j2\varphi_2} e^{-j2\varphi_3} + r_1 r_3 e^{-j2\varphi_2} e^{-j2\varphi_3} + r_0 r_3 e^{-j2\varphi_1} e^{-j2\varphi_2} e^{-j2\varphi_3}} \right|^2 \end{aligned} \quad (12)$$

REFERENCES

- [1] M. Schneider, "Automotive radar-status and trends," in *Proc. German Microw. Conf.*, 2005, pp. 144–147.
- [2] C. Fischer, F. Ruf, H.-L. Bloecher, J. Dickmann, and W. Menzel, "Evaluation of different super-resolution techniques for automotive applications," in *Proc. ET Int. Conf. Radar Syst. Radar*, 2012, pp. 1–6.
- [3] J. Hasch, E. Topak, R. Schnabel, T. Zwick, R. Weigel, and C. Waldschmidt, "Millimeter-wave technology for automotive radar sensors in the 77 GHz frequency band," *IEEE Trans. Microw. Theory Techn.*, vol. 60, no. 3, pp. 845–860, Mar. 2012.
- [4] M. Al Henawy and M. Schneider, "Integrated antennas in eWLB packages for 77 GHz and 79 GHz automotive radar sensors," in *Proc. 41st Eur. Microw. Conf.*, Oct. 2011, pp. 1312–1315.
- [5] F. Pfeiffer and E. M. Biebl, "Inductive compensation of high-permittivity coatings on automobile long-range radar radomes," *IEEE Trans. Microw. Theory Techn.*, vol. 57, no. 11, pp. 2627–2632, Nov. 2009.
- [6] R. H. Rasshofer and K. Gresser, "Automotive radar and lidar systems for next generation driver assistance functions," *Adv. Radio Sci.*, vol. 3, no. 4, pp. 205–209, May 2005.
- [7] J. Park, H. Ryu, K.-W. Ha, J.-G. Kim, and D. Baek, "76–81-GHz CMOS transmitter with a phase-locked-loop-based multichirp modulator for automotive radar," *IEEE Trans. Microw. Theory Techn.*, vol. 63, no. 4, pp. 1399–1408, Apr. 2015.
- [8] R. Schneider, H.-L. Blocher, and K. M. Strohm, "KOKON—automotive high frequency technology at 77/79 GHz," in *Proc. Eur. Microw. Conf.*, 2007, pp. 1526–1529.
- [9] M. Goppelt, H.-L. Blöcher, and W. Menzel, "Automotive radar-investigation of mutual interference mechanisms," *Adv. Radio Sci.*, vol. 8, pp. 55–60, Sep. 2010.
- [10] W. Menzel and A. Moebius, "Antenna concepts for millimeter-wave automotive radar sensors," *Proc. IEEE*, vol. 100, no. 7, pp. 2372–2379, Jul. 2012.
- [11] M. Gashinova, E. Hoare, and A. Stove, "Predicted sensitivity of a 300 GHz FMCW radar to pedestrians," in *Proc. 46th Eur. Microw. Conf. (EuMC)*, Oct. 2016, pp. 1497–1500.
- [12] D. Jasteh, E. G. Hoare, M. Cherniakov, and M. Gashinova, "Experimental low-terahertz radar image analysis for automotive terrain sensing," *IEEE Geosci. Remote Sens. Lett.*, vol. 13, no. 4, pp. 490–494, Apr. 2016.
- [13] F. Norouzian *et al.*, "Low-THz transmission through water-containing contaminants on antenna radome," *IEEE Trans. Terahertz Sci. Technol.*, vol. 8, no. 1, pp. 63–75, Jan. 2018.
- [14] K. Konstantinidis *et al.*, "Low-THz dielectric lens antenna with integrated waveguide feed," *IEEE Trans. Terahertz Sci. Technol.*, vol. 7, no. 5, pp. 572–581, Sep. 2017.
- [15] D. R. Vizard, E. G. Hoare, M. Gashinova, and M. Cherniakov, "Applications of low THz frequency extenders for vector network analyzers," in *Proc. IEEE Radio Antenna Days Indian Ocean (RADIO)*, Oct. 2018, pp. 1–2.
- [16] D. R. Vizard, E. G. Hoare, M. Gashinova, and M. Cherniakov, "A novel 670 GHz hybrid frequency extender for portable automotive radar applications," in *Proc. 18th Int. Radar Symp. (IRS)*, Jun. 2017, pp. 1–5.
- [17] L. Daniel *et al.*, "Application of Doppler beam sharpening for azimuth refinement in prospective low-THz automotive radars," *IET Radar, Sonar Navigat.*, vol. 12, no. 10, pp. 1121–1130, Oct. 2018.
- [18] E. Marchetti *et al.*, "Radar cross-section of pedestrians in the low-THz band," *IET Radar, Sonar Navigat.*, vol. 12, no. 10, pp. 1104–1113, Oct. 2018.
- [19] Y. Xiao *et al.*, "Transmissivity through automotive bumpers at mm-wave and low-THz frequencies," presented at the Int. Radar Symp. (IRS) 2019, Ulm, Germany, Jun. 2019.
- [20] F. Norouzian *et al.*, "Transmission through uniform layer of ice at low-THz frequencies," in *Proc. Eur. Radar Conf. (EURAD)*, Oct. 2017, pp. 211–214.
- [21] S. Sabery, F. Norouzian, P. Gardner, E. Hoare, M. Cherniakov, and M. Gashinova, "Signal reduction by tree leaves in low-THz automotive radar," in *Proc. 15th Eur. Radar Conf. (EuRAD)*, Sep. 2018, pp. 1445–1448.
- [22] R. Du, F. Norouzian, E. Marchetti, B. Willetts, M. Gashinova, and M. Cherniakov, "Characterisation of attenuation by sand in low-THz band," in *Proc. IEEE Radar Conf. (RadarConf)*, May 2017, pp. 0294–0297.
- [23] F. Norouzian *et al.*, "Low-THz wave snow attenuation," in *Proc. Int. Conf. Radar (RADAR)*, 2018, pp. 1–4.
- [24] J. F. Federici *et al.*, "THz imaging and sensing for security applications—Explosives, weapons and drugs," *Semicond. Sci. Technol.*, vol. 20, no. 7, pp. S266–S280, Jul. 2005.
- [25] R. Appleby and H. B. Wallace, "Standoff detection of weapons and contraband in the 100 GHz to 1 THz region," *IEEE Trans. Antennas Propag.*, vol. 55, no. 11, pp. 2944–2956, Nov. 2007.
- [26] A. Panwar, A. Singh, A. Kumar, and H. Kim, "Terahertz imaging system for biomedical applications: Current status," *Syst.*, vol. 28, p. 44, Apr. 2013.
- [27] J. Dickmann *et al.*, "Making bertha see even more: Radar contribution," *IEEE Access*, vol. 3, pp. 1233–1247, 2015.
- [28] H.-L. Bloecher, A. Sailer, G. Rollmann, and J. Dickmann, "79 GHz UWB automotive short range radar—spectrum allocation and technology trends," *Adv. Radio Sci.*, vol. 7, pp. 61–65, May 2009.
- [29] F. Norouzian *et al.*, "Rain attenuation at millimeter wave and low-THz frequencies," *IEEE Trans. Antennas Propag.*, vol. 68, no. 1, pp. 421–431, Jan. 2020.
- [30] M. Köhler, J. Hasch, H. L. Blöcher, and L.-P. Schmidt, "Feasibility of automotive radar at frequencies beyond 100 GHz," *Int. J. Microw. Wireless Technol.*, vol. 5, no. 1, pp. 49–54, Feb. 2013.
- [31] F. Norouzian *et al.*, "Experimental study on low-THz automotive radar signal attenuation during snowfall," *IET Radar, Sonar Navigat.*, vol. 13, no. 9, pp. 1421–1427, Sep. 2019.
- [32] F. Norouzian, E. Hoare, E. Marchetti, M. Cherniakov, and M. Gashinova, "Next generation, low-THz automotive radar—the potential for frequencies above 100 GHz," in *Proc. 20th Int. Radar Symp. (IRS)*, 2019, pp. 1–7.
- [33] F. Fitzek, Z. Abou-Chahine, R. H. Rasshofer, and E. M. Biebl, "Automotive radome design—fishnet structure for 79 GHz," in *Proc. German Microw. Conf.*, 2010, pp. 146–149.
- [34] F. Fitzek and R. H. Rasshofer, "Automotive radome design—reflection reduction of stratified media," *IEEE Antennas Wireless Propag. Lett.*, vol. 8, pp. 1076–1079, 2009.
- [35] F. Fitzek, R. H. Raßhofer, and E. M. Biebl, "Broadband matching of high-permittivity coatings with frequency selective surfaces," in *Proc. Microw. Conf. (GeMIC)*, Darmstadt, Germany, 2011, pp. 1–4.
- [36] F. Fitzek, R. H. Rasshofer, and E. M. Biebl, "Comparison of matching layers for automotive radome design," *Adv. Radio Sci.*, vol. 8, no. 3, pp. 49–54, Sep. 2010.
- [37] N. Chen, R. Gourova, O. A. Krasnov, and A. Yarovoy, "The influence of the water-covered dielectric radome on 77GHz automotive radar signals," in *Proc. Eur. Radar Conf. (EURAD)*, Oct. 2017, pp. 139–142.
- [38] D. J. Kozakoff, *Analysis of Radome-Enclosed Antennas*. Norwood, MA, USA: Artech House, 2010.
- [39] H. Bloecher, C. Fischer, and A. Sailer, "Prerequisites of mmW automotive radar specification, platform integration and operation," in *Proc. Eur. Radar Conf.*, 2013, pp. 192–195.
- [40] M. N. Sadiku, *Elements of Electromagnetics*. London, U.K.: Oxford Univ. Press, 2014.
- [41] Y.-S. Jin, G.-J. Kim, and S.-G. Jeon, "Terahertz dielectric properties of polymers," *J. Korean Phys. Soc.*, vol. 49, no. 2, pp. 513–517, 2006.
- [42] M. Naftaly and R. E. Miles, "Terahertz time-domain spectroscopy for material characterization," *Proc. IEEE*, vol. 95, no. 8, pp. 1658–1665, Aug. 2007.
- [43] R. Piesiewicz, C. Jansen, S. Wietzke, D. Mittleman, M. Koch, and T. Kürner, "Properties of building and plastic materials in the THz range," *Int. J. Infr. Millim. Waves*, vol. 28, no. 5, pp. 363–371, Apr. 2007.
- [44] M. M. Davoodi, S. M. Sapuan, D. Ahmad, A. Aidy, A. Khalina, and M. Jonoobi, "Concept selection of car bumper beam with developed hybrid bio-composite material," *Mater. Des.*, vol. 32, no. 10, pp. 4857–4865, Dec. 2011.
- [45] J. Marzbanrad, M. Alijanpour, and M. S. Kiasat, "Design and analysis of an automotive bumper beam in low-speed frontal crashes," *Thin-Walled Struct.*, vol. 47, nos. 8–9, pp. 902–911, Aug. 2009.
- [46] E. Emilsson, "Radar transparency and paint compatibility—A study of automobile bumper and bumper-skin complex permittivities for 77 GHz microwaves," M.S. thesis, Chalmers Univ. Technol., Gothenburg, Sweden, 2017.
- [47] T. D. Dorney, R. G. Baraniuk, and D. M. Mittleman, "Material parameter estimation with terahertz time-domain spectroscopy," *J. Opt. Soc. Amer. A, Opt. Image Sci.*, vol. 18, no. 7, pp. 1562–1571, Jul. 2001.
- [48] L. Duvillaret, F. Garet, and J.-L. Coutaz, "A reliable method for extraction of material parameters in terahertz time-domain spectroscopy," *IEEE J. Sel. Topics Quantum Electron.*, vol. 2, no. 3, pp. 739–746, Sep. 1996.
- [49] F. Norouzian *et al.*, "Monostatic and bistatic reflectivity measurements of radar absorbers at low-THz frequency," in *Proc. Eur. Radar Conf. (EURAD)*, 2016, pp. 117–120.

- [50] F. Norouzian *et al.*, "Signal reduction due to radome contamination in low-THz automotive radar," in *Proc. IEEE Radar Conf. (RadarConf)*, May 2016, pp. 1–4.
- [51] E-MWDO. *Elva-1.Com*. Accessed: Mar. 31, 2020. [Online]. Available: <http://www.elva-1.com>
- [52] J. Hammler, A. J. Gallant, and C. Balocco, "Free-space permittivity measurement at terahertz frequencies with a vector network analyzer," *IEEE Trans. Terahertz Sci. Technol.*, vol. 6, no. 6, pp. 817–823, Nov. 2016.
- [53] S. Krimi, J. Klier, J. Jonuscheit, G. von Freymann, R. Urbansky, and R. Beigang, "Highly accurate thickness measurement of multi-layered automotive paints using terahertz technology," *Appl. Phys. Lett.*, vol. 109, no. 2, Jul. 2016, Art. no. 021105.
- [54] T. Tosaka, K. Fujii, K. Fukunaga, and A. Kasamatsu, "Development of complex relative permittivity measurement system based on free-space in 220–330-GHz range," *IEEE Trans. THz Sci. Technol.*, vol. 5, no. 1, pp. 102–109, Oct. 2015.
- [55] A. Melzer, A. Onic, F. Starzer, and M. Huemer, "Short-range leakage cancellation in FMCW radar transceivers using an artificial on-chip target," *IEEE J. Sel. Topics Signal Process.*, vol. 9, no. 8, pp. 1650–1660, Dec. 2015.



Yang Xiao received the M.Eng. degree in electronic and communication engineering from Tianjin University, China. She is currently pursuing the Ph.D. degree in low-THz automotive radar with the Microwave Integrated Systems Laboratory, University of Birmingham. Her research interests include the image segmentation using deep learning and feature extraction in automotive radar application, theoretical modeling of signal propagation, and practical experimental work on Low-THz radar systems.



Fatemeh Norouzian received the Ph.D. degree in electronic and communication engineering from the University of Birmingham in 2015. Her Ph.D. thesis was on developing a methodology to design high-efficiency power amplifiers for cognitive radio communication systems. She then continued at the University of Birmingham, as a Research Fellow. Her research interests include radar technology at system level, low-THz short-range sensing, EM theory, modeling and characterization of signal propagation through diverse media, and automotive radar signal processing.



Edward G. Hoare (Senior Member, IEEE) received the Ph.D. degree in over-the-horizon radar from the University of Birmingham. He undertook an apprenticeship at The Royal Radar Establishment, College of Electronics, Malvern, U.K., and after a spell in industry joined the School of Electronic, Electrical, and Computer Engineering, University of Birmingham. Since that time, he has been involved in teaching, design, and research into radar systems and antennas covering frequencies from 2 MHz to over 670 GHz, including non co-operative bistatic radar, atmospheric radar acoustic sounding, automotive radar, and low-THz radar. Over the past 12 years, he has provided antenna and millimetre-wave radar consultancy to Jaguar Land Rover and Ford Motor Company. He holds a number of patents in automotive radar. He was a member of the European Automotive Radar Standards Group.



Emidio Marchetti received the M.Eng. degree in communication engineering from 'La Sapienza' University of Rome, Italy, and the M.Sc. degree in RF and microwave engineering and the Ph.D. degree in radar systems from the University of Birmingham (UoB), U.K. He is a Research Fellow at the Microwave Integrated Systems Laboratory, UoB. His research interests include automotive radar systems, THz sensing, ISAR imaging, and spaceborne radar systems.



Marina Gashinova received the M.Sc. degree in math from St-Petersburg State University in 1991 and the Ph.D. degree in physics and math from St-Petersburg Electrotechnical University, Russia, in 2003. In 2006, she joined the Microwave Integrated System Laboratory (MISL), University of Birmingham (UoB), where she is the Chair of Pervasive Sensing. She is also the Head of the Pervasive Sensing Group, MISL, leading a number of research projects on automotive sensing and THz sensing. Her area

of interests include active and passive radar, imaging THz sensing for ground and spaceborne scene assessments, cognitive radar, and deep neural networks classification.



Mikhail Cherniakov graduated from Moscow Technical University in 1974. He received the Ph.D. degree in 1980 and the D.Sc. degree in 1992. He was a Full Professor in 1993. In 1994, he was a Visiting Professor with the University of Cambridge. In 1995, he moved to the University of Queensland, Australia. In 2000, he joined the School of EEESE, Birmingham. Here, he founded the Microwave Integrated Systems Laboratory. He is the Chair of the Aerospace and Electronic Systems, University of Birmingham, U.K, with more than 40 years' experience on the R&D in radar systems. His research interests are in forward scatter and multistatic radar, active and passive radar, automotive, and short range sensors. He is the author/editor/coauthor of five books. He has more than 250 peer-reviewed publications. In 2017, he received the Christian Hülsmeier Award for his achievements in radar research and education.